Electronic supplementary materials

For https://doi.org/10.1631/jzus.A2200525

Two-dimensional plane-strain consolidation for unsaturated soils under non-uniform trapezoidal loads

Chengjia TANG[1], Lei WANG[1], Sidong SHEN[1], Minjie WEN[2], Annan ZHOU[3]

[1]*School of Urban Railway Transportation, Shanghai University of Engineering Science, Shanghai 201620, China*
[2]*MOE Key Laboratory of Soft Soils and Geoenvironmental Engineering, Zhejiang University, Hangzhou 310058, China*
[3]*School of Civil, Environmental and Chemical Engineering, Royal Melbourne Institute of Technology (RMIT), Melbourne VIC 3001, Australia*

Section S1

Fig. S1 and Fig. S2 outline the function of the external load $g(t)$ and $f(x)$.

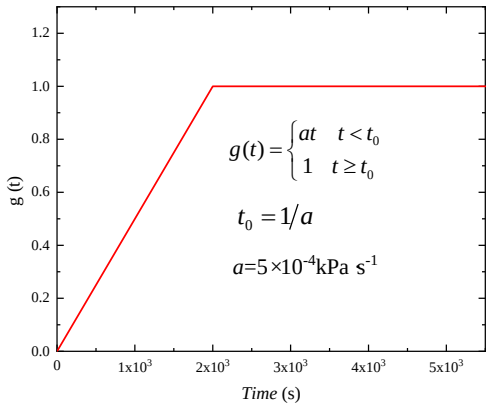

Fig. S1 The function g(*t*) with time *t*

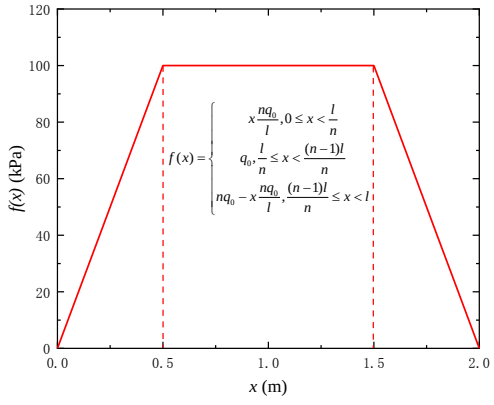

Fig. S2 The function f(*x*) with the lateral location *x*

Section S2

The governing equations are as follows:

$$\frac{\partial u_a}{\partial t}=-C_a\frac{\partial u_w}{\partial t}-C_{v_x}^a\frac{\partial^2 u_a}{\partial x^2}-C_{v_z}^a\frac{\partial^2 u_a}{\partial z^2}+C_\sigma^a\frac{\partial \sigma_z}{\partial t} \quad \text{(S1)}$$

$$\frac{\partial u_w}{\partial t}=-C_w\frac{\partial u_a}{\partial t}-C_{v_x}^w\frac{\partial^2 u_w}{\partial x^2}-C_{v_z}^w\frac{\partial^2 u_w}{\partial z^2}+C_\sigma^w\frac{\partial \sigma_z}{\partial t} \quad \text{(S2)}$$

The specific expressions of these parameters are:

$$C_a=\frac{m_2^a}{2m_1^a-m_2^a-\frac{n_0(1-S_{r0})}{(u_a^0+u_{atm})}} \quad \text{(S3a)}$$

$$C_{v_x}^a=\frac{k_{a_x}R\Theta}{gM[(u_a^0+u_{atm})(2m_1^a-m_2^a)-n_0(1-S_{r0})]} \quad \text{(S3b)}$$

$$C_{v_z}^a=\frac{k_{a_z}R\Theta}{gM[(u_a^0+u_{atm})(2m_1^a-m_2^a)-n_0(1-S_{r0})]} \quad \text{(S3c)}$$

$$C_\sigma^a=\frac{m_1^a}{2m_1^a-m_2^a-\frac{n_0(1-S_{r0})}{(u_a^0+u_{atm})}} \quad \text{(S3d)}$$

$$C_w=\frac{m_2^w/2m_1^w-1}{m_2^w/2m_1^w} \quad \text{(S3e)}$$

$$C_{v_x}^w=\frac{k_{w_x}}{\gamma_w m_2^w} \quad \text{(S3f)}$$

$$C_{v_z}^w=\frac{k_{w_z}}{\gamma_w m_2^w} \quad \text{(S3g)}$$

$$C_\sigma^w=\frac{m_1^w}{m_2^w} \quad \text{(S3h)}$$

m_1^w and m_2^w are the coefficients of volume change for the water phase; m_1^a and m_2^a are the coefficients of volume change for the air phase; k_{a_x} and k_{w_x} are the permeability coefficients for the air and water phases in the x-direction; k_{a_z} and k_{w_z} are the permeability coefficients of the air and water phases in the z-direction; γ_w is the unit weight of water, $\gamma_w = 9.8\mathrm{kN}\cdot\mathrm{m}^{-3}$; g is the acceleration of gravity, $g = 9.8\,\mathrm{m/s^2}$; S_{r0} is the initial saturation; n_0 is the initial porosity; M is the air molecular modulus, $M = 0.029\mathrm{kg}\cdot\mathrm{mol}^{-1}$; u_a^0 is the initial excess pore-air pressures; u_{atm} is the atmospheric pressure; R is the universal air constant, $R = 8.314\,\mathrm{J/mol/K}$; Θ is the absolute temperature.

Section S3

The expressions of the boundary conditions are expressed as follows:
Top boundary:

$$u_a(x,0,t) = 0, \quad u_w(x,0,t) = 0 \tag{S4}$$

Bottom boundary:

$$\frac{\partial u_a(x,h,t)}{\partial z} = 0, \quad \frac{\partial u_w(x,h,t)}{\partial z} = 0 \tag{S5}$$

Lateral boundary:

$$u_a(0,z,t) = u_a(l,z,t) = \\ u_w(0,z,t) = u_w(l,z,t) = 0 \tag{S6}$$

If the equations were derived assuming two-way vertical drainage, the boundary conditions are expressed as follows.

$$u_a(x,h,t) = 0, u_w(x,h,t) = 0 \tag{S7}$$

Section S4

The governing equations are as follows:

$$\frac{\partial u_a}{\partial \mathrm{t}} = -C_a\frac{\partial u_w}{\partial \mathrm{t}} - C_{v_x}^a\frac{\partial^2 u_a}{\partial \mathrm{x}^2} - C_{v_z}^a\frac{\partial^2 u_a}{\partial \mathrm{z}^2} + C_\sigma^a\frac{\partial \sigma_z}{\partial \mathrm{t}} \tag{S8}$$

$$\frac{\partial u_w}{\partial \mathrm{t}} = -C_w\frac{\partial u_a}{\partial \mathrm{t}} - C_{v_x}^w\frac{\partial^2 u_w}{\partial \mathrm{x}^2} - C_{v_z}^w\frac{\partial^2 u_w}{\partial \mathrm{z}^2} + C_\sigma^w\frac{\partial \sigma_z}{\partial \mathrm{t}} \tag{S9}$$

According to the lateral boundary, the variables Z in the governing equations are separated out by the Fourier series to obtain the following equations:

$$u_a(x,z,t) = \sum_{k=1}^{\infty} U_a(x,t)\sin[Kz] \tag{S10}$$

$$u_w(x,z,t) = \sum_{k=1}^{\infty} U_w(x,t)\sin[Kz] \tag{S11}$$

The first-order derivative of Eqs. (S10) and (S11) with respect to t are obtained as follows

$$\frac{\partial u_a(x,z,t)}{\partial t} = \sum_{k=1}^{\infty}\frac{\partial U_a(x,t)}{\partial t}\sin[Kz] \tag{S12}$$
$$\frac{\partial u_w(x,z,t)}{\partial t} = \sum_{k=1}^{\infty}\frac{\partial U_w(x,t)}{\partial t}\sin[Kz] \tag{S13}$$

The second-order derivative of Eqs. (S10) and (S11) with respect to x and z are obtained as follows

$$\frac{\partial^2 u_a(x,z,t)}{\partial^2 x} = \sum_{k=1}^{\infty}\frac{\partial^2 U_a(x,t)}{\partial^2 x}\sin[Kz] \tag{S14}$$
$$\frac{\partial^2 u_w(x,z,t)}{\partial^2 x} = \sum_{k=1}^{\infty}\frac{\partial^2 U_w(x,t)}{\partial^2 x}\sin[Kz] \tag{S15}$$
$$\frac{\partial^2 u_a(x,z,t)}{\partial^2 z} = -\sum_{k=1}^{\infty} U_a[K]^2\sin[\frac{(2k+1)\pi}{2h}z] \tag{S16}$$
$$\frac{\partial^2 u_w(x,z,t)}{\partial^2 z} = -\sum_{k=1}^{\infty} U_w[K]^2\sin[\frac{(2k+1)\pi}{2h}z] \tag{S17}$$

Substituting Eq. (S12) to (S17) into governing equations gives

$$\frac{\partial U_a}{\partial t} = -C_a\frac{\partial U_w}{\partial t} - C_{v_x}^a\frac{\partial^2 U_a}{\partial^2 x} + C_{v_z}^a U_a[K]^2 + \frac{4\sigma_\sigma^a}{(2k+1)\pi}\frac{\partial(\sigma z)}{\partial \mathrm{t}} \tag{S18}$$

$$\frac{\partial U_w}{\partial t} = -C_a\frac{\partial U_a}{\partial t} - C_{v_x}^w\frac{\partial^2 U_w}{\partial^2 x} + C_{v_z}^w U_w[K]^2 + \frac{4\sigma_\sigma^w}{(2k+1)\pi}\frac{\partial(\sigma z)}{\partial \mathrm{t}} \tag{S19}$$

Conducting Laplace transform on Eqs. (S18) and (S19) leads to

$$\widetilde{U}_w = -\frac{C_{v_x}^a}{sC_a}\frac{\partial^2\widetilde{U}_a}{\partial x^2} + \frac{C_{v_z}^a - \mathrm{s}}{sC_a}\widetilde{U}_a + \frac{U_a^0 + C_a U_w^0}{sC_a} + \frac{4\sigma_\sigma^a}{\mathrm{sC_a}(2k+1)\pi}Q(x,s) \tag{S20}$$

$$\widetilde{U}_a = -\frac{C_{v_x}^w}{sC_w}\frac{\partial^2\widetilde{U}_w}{\partial x^2} + \frac{C_{v_z}^w - \mathrm{s}}{sC_w}\widetilde{U}_w + \frac{U_w^0 + C_w U_a^0}{sC_w} + \frac{4\sigma_\sigma^w}{sC_w(2k+1)\pi}Q(x,s) \tag{S21}$$

where, $U_a^0 = \frac{4u_a^0}{(2\mathrm{k}+1)\pi}$, $U_w^0 = \frac{4u_w^0}{(2\mathrm{k}+1)\pi}$.

Implementing the second-order partial derivative of Eq. (S9+11) with respect to *x* gives

$$\frac{\partial^2 \widetilde{U}_w}{\partial x^2} = -\frac{C_{v_x}^a}{sC_a}\frac{\partial^4 \widetilde{U}_a}{\partial x^4} + \frac{[C_{v_z}^a - s]}{sC_a}\frac{\partial^2 \widetilde{U}_a}{\partial x^2} \quad \text{(S22)}$$

Substitute Eqs. (S18) and (S20) into Eq. (S21) has

$$a_1\frac{\partial^4 \widetilde{U}_a}{\partial x^4} + \mathrm{a}_2\frac{\partial^2 \widetilde{U}_a}{\partial x^2} + \mathrm{a}_3\widetilde{U}_a + \mathrm{a}_4 = 0 \quad \text{(S23)}$$

where, $a_1 = \frac{C_{v_x}^a C_{v_x}^w}{s^2 C_a C_w}$,
$a_2 = -\frac{C_{v_x}^w(C_{v_z}^a k^2 - s) + C_{v_x}^a(C_{v_z}^w k^2 - s)}{s^2 C_a C_w}$,
$a_3 = \frac{(C_{v_z}^a k^2 - s)(C_{v_z}^w k^2 - s) - s^2 C_a C_w}{s^2 C_a C_w}$,
$a_4 = \frac{(C_{v_z}^w \mathrm{k}^2 - s)(U_a^0 + C_a U_w^0)}{s^2 C_a C_w} + \frac{U_w^0 + C_w U_a^0}{sC_w} + [\frac{\sigma_\sigma^a(C_{v_z}^w k^2 - s)}{sC_a} + \sigma_\sigma^w]\frac{4Q(x,s)}{sC_w(2k+1)\pi}$.

The general solution of four-order ordinary differential Eq. (S23) is

$$\widetilde{U}_a = \mathrm{C}_1 e^{\xi x} + \mathrm{C}_2 e^{-\xi x} + \mathrm{D}_1 e^{\eta x} + \mathrm{D}_2 e^{-\eta x} - \frac{a_4}{a_3} \quad \text{(S24)}$$

where, $\xi = \sqrt{-(a_2 + \sqrt{{a_2}^2 - 4a_1a_3})/2a_1}$, $\eta = \sqrt{-(a_2 - \sqrt{{a_2}^2 - 4a_1a_3})/2a_1}$, and $\mathrm{C}_1, \mathrm{C}_2, \mathrm{D}_1$, and D_2 are the pending coefficients on n and s determined by the boundary conditions.

The first-order and second-order partial derivatives of Eq. (S24) with respect to *x* can be obtained as follow:

$$\frac{\partial \widetilde{U}_a}{\partial x} = \xi\mathrm{C}_1 e^{\xi x} - \xi\mathrm{C}_2 e^{-\xi x} + \eta\mathrm{D}_1 e^{\eta x} - \eta\mathrm{D}_2 e^{-\eta x} \quad \text{(S25)}$$

$$\frac{\partial^2 \widetilde{U}_a}{\partial x^2} = \xi^2\mathrm{C}_1 e^{\xi x} + \xi^2\mathrm{C}_2 e^{-\xi x} + \eta^2\mathrm{D}_1 e^{\eta x} + \eta^2\mathrm{D}_2 e^{-\eta x} \quad \text{(S26)}$$

Substitute Eqs (S25) and (S26) into Eq. (S20) yields,

$$\widetilde{U}_w = \mathrm{a}_5\mathrm{C}_1 e^{\xi x} + \mathrm{a}_5\mathrm{C}_2 e^{-\xi x} + \mathrm{a}_6\mathrm{D}_1 e^{\eta x} + \mathrm{a}_6\mathrm{D}_2 e^{-\eta x} + \mathrm{a}_7 \quad \text{(S27)}$$

where, $a_5 = \frac{(C_{v_z}^a K^2 - s) - \xi^2 C_{v_x}^a}{sC_a}$, $a_6 = \frac{(C_{v_z}^a K^2 - s) - \eta^2 C_{v_x}^a}{sC_a}$, $a_7 = -\frac{a_4(C_{v_z}^a K^2 - s)}{sa_3 C_a} + \frac{U_a^0 + C_a U_w^0}{sC_a} + \frac{4\sigma_\sigma^a}{sC_a(2k+1)\pi}Q(x,s)$.

Implementing the first-order partial derivative of Eq. (S27) with regard to *x* gives

$$\frac{\partial \widetilde{U}_w}{\partial x} = \mathrm{a}_5\xi\mathrm{C}_1 e^{\xi x} - \mathrm{a}_5\xi\mathrm{C}_2 e^{-\xi x} + \mathrm{a}_6\eta\mathrm{D}_1 e^{\eta x} - \mathrm{a}_6\eta\mathrm{D}_2 e^{-\eta x} \quad \text{(S28)}$$

Substitute Eqs. (S24), (S25), (S27), (S28) into the top and bottom boundary conditions has,

$$\mathrm{C}_1 + \mathrm{C}_2 + \mathrm{D}_1 + \mathrm{D}_2 = \frac{a_4}{a_3} \quad \text{(S29a)}$$

$$\mathrm{C}_1 e^{\xi l} + \mathrm{C}_2 e^{-\xi l} + \mathrm{D}_1 e^{\eta l} + \mathrm{D}_2 e^{-\eta l} = \frac{a_4}{a_3} \quad \text{(S29b)}$$

$$\mathrm{a}_5\mathrm{C}_1 + \mathrm{a}_5\mathrm{C}_2 + \mathrm{a}_6\mathrm{D}_1 + \mathrm{a}_6\mathrm{D}_2 = -\mathrm{a}_7 \quad \text{(S29c)}$$

$$\mathrm{a}_5\mathrm{C}_1 e^{\xi l} + \mathrm{a}_5\mathrm{C}_2 e^{-\xi l} + \mathrm{a}_6\mathrm{D}_1 e^{\eta l} + \mathrm{a}_6\mathrm{D}_2 e^{-\eta l} = -\mathrm{a}_7 \quad \text{(S29d)}$$

Solving the variable primary Eq. (S29) leads to

$$\mathrm{C}_1 = -\frac{\mathrm{a}_4\mathrm{a}_6 + \mathrm{a}_3\mathrm{a}_7}{\mathrm{a}_3(\mathrm{a}_5 - \mathrm{a}_6)(1 + e^{\xi l})} \quad \text{(S30a)}$$

$$\mathrm{C}_2 = -\frac{(\mathrm{a}_4\mathrm{a}_6 + \mathrm{a}_3\mathrm{a}_7)e^{\xi l}}{\mathrm{a}_3(\mathrm{a}_5 - \mathrm{a}_6)(1 + e^{\xi l})} \quad \text{(S30b)}$$

$$\mathrm{D}_1 = \frac{\mathrm{a}_4\mathrm{a}_5 + \mathrm{a}_3\mathrm{a}_7}{\mathrm{a}_3(\mathrm{a}_5 - \mathrm{a}_6)(1 + e^{\eta l})} \quad \text{(S30c)}$$

$$\mathrm{D}_1 = \frac{(\mathrm{a}_4\mathrm{a}_5 + \mathrm{a}_3\mathrm{a}_7)e^{\eta l}}{\mathrm{a}_3(\mathrm{a}_5 - \mathrm{a}_6)(1 + e^{\eta l})} \quad \text{(S30d)}$$

Substitute (S30) into Eq. (S24) and (S27) has,

$$\widetilde{U}_a = -\frac{(\mathrm{a}_4\mathrm{a}_6 + \mathrm{a}_3\mathrm{a}_7)\left(e^{\xi x} + e^{\xi l - \xi \mathrm{x}}\right)}{\mathrm{a}_3(\mathrm{a}_5 - \mathrm{a}_6)(1 + e^{\xi l})} + \frac{(\mathrm{a}_4\mathrm{a}_5 + \mathrm{a}_3\mathrm{a}_7)(e^{\eta x} + e^{\eta l - \eta x})}{\mathrm{a}_3(\mathrm{a}_5 - \mathrm{a}_6)(1 + e^{\eta l})} - \frac{a_4}{a_3} \quad \text{(S31a)}$$

$$\widetilde{U}_w = -\frac{a_5(\mathrm{a}_4\mathrm{a}_6 + \mathrm{a}_3\mathrm{a}_7)\left(e^{\xi x} + e^{\xi l - \xi x}\right)}{\mathrm{a}_3(\mathrm{a}_5 - \mathrm{a}_6)(1 + e^{\xi l})} + \frac{a_6(\mathrm{a}_4\mathrm{a}_5 + \mathrm{a}_3\mathrm{a}_7)(e^{\eta x} + e^{\eta l - \eta x})}{\mathrm{a}_3(\mathrm{a}_5 - \mathrm{a}_6)(1 + e^{\eta l})} + \mathrm{a}_7 \quad \text{(S31b)}$$

Since the lateral boundaries of one-way vertical drainage and two-way vertical drainage are the same. Therefore, the rest of derivation process is same as the derivation process of the semi-analytic solution in the

case of one-way drainage.

So the solutions to the governing equation in the case of two-way drainage can be obtained as Eqs. (S32) and (S9+24)

$$u_a(x,z,t) = L^{-1}[\sum_{k=1}^{\infty} \widetilde{U}_a(x,s)\sin(K_0 z)] \quad \text{(S32)}$$
$$u_w(x,z,t) = L^{-1}[\sum_{k=1}^{\infty} \widetilde{U}_w(x,s)\sin(K_0 z)] \quad \text{(S33)}$$

Section S5

Fig. S3 demonstrates the exact location of the calculated points under the trapezoidal load, which is the reference model of Section 5.1.

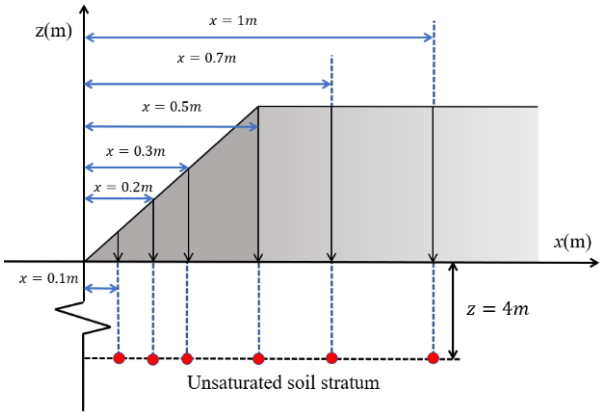

Fig. S3 Schematic diagram of different calculated points

Fig. S4 shows the settlement calculation results at different calculation points, and it can be found that the settlement under the pavement is significantly larger than that under the road shoulder. And when x is adopted as 0.1, 0.2 and 0.3, the settlement under the road shoulder is 20%, 40%, and 60% of the settlement under the pavement, respectively. Although the settlement under the pavement is almost consistent, the rates of the settlement curves are different. Starting from $t = 10^{3.5}s$ (please Fig. 3), the pore air pressure and pore water pressure reach their maximum values successively. As shown in Fig. S4, the two plateau periods are due to the pore pressure reaching a maximum, and the plateau periods in the settling curve ends as the pore pressure dissipates. The further the calculation point of the road surface is from the lateral boundary, the later the pore pressure dissipates. When the excess pore pressure near the boundary close to finish dissipation, the excess pore pressure in the middle of the soil can dissipate fast. This results in a consistent time at which settlement is completed, but different rates of settlement during the process.

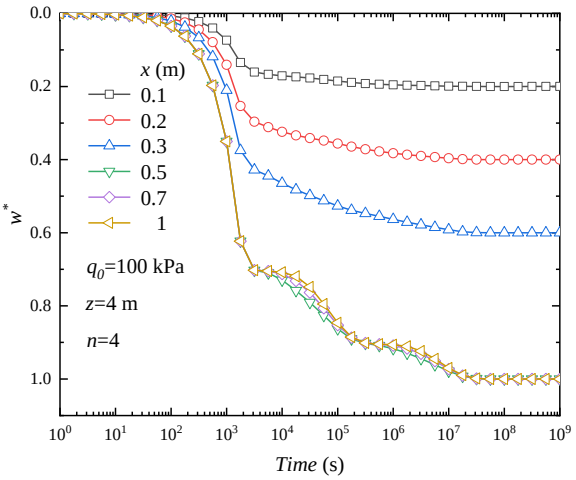

Fig. S4 The variation of normalized settlement under non-uniform loads for different investigated widths x

Fig. S5 and Fig. S6 show the variation of excess pore pressure along the depth of unsaturated soil stratum. x=1 is the centerline of the embankment, x=0.5 is the junction line between the pavement and the shoulder, and x=0.2 is located at the shoulder. As the analysis of Fig. 3, the maximum value of excess pore pressure is the same for x=1 and x=0.5; the maximum value of excess pore pressure under the shoulder is smaller.

Since the top is the permeable boundary, the closer to the top, the lower the excess pore air pressure. When the excess pore air pressure starts to dissipate, it can be found that the excess pore air pressure near the top starts to dissipate earliest. The plateau period of the excess pore water pressure is not obvious compared to the Fig. 3. When the excess pore air pressure starts to dissipate, the excess pore water pressure ends the plateau period and starts to increase. The excess pore air pressure firstly starts to dissipate from the top, and the corresponding excess pore water pressure starts to increase from the top after the plateau period, too.

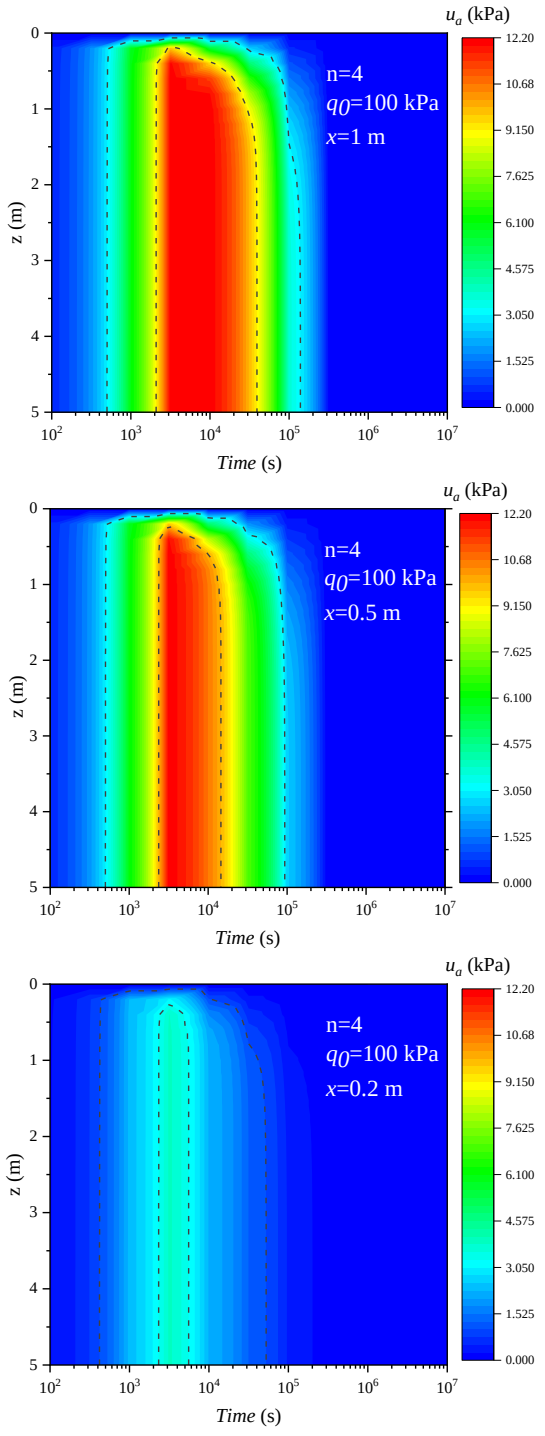

Fig. S5 2D plots of excess pore air pressure varying along the depth of unsaturated soil stratum

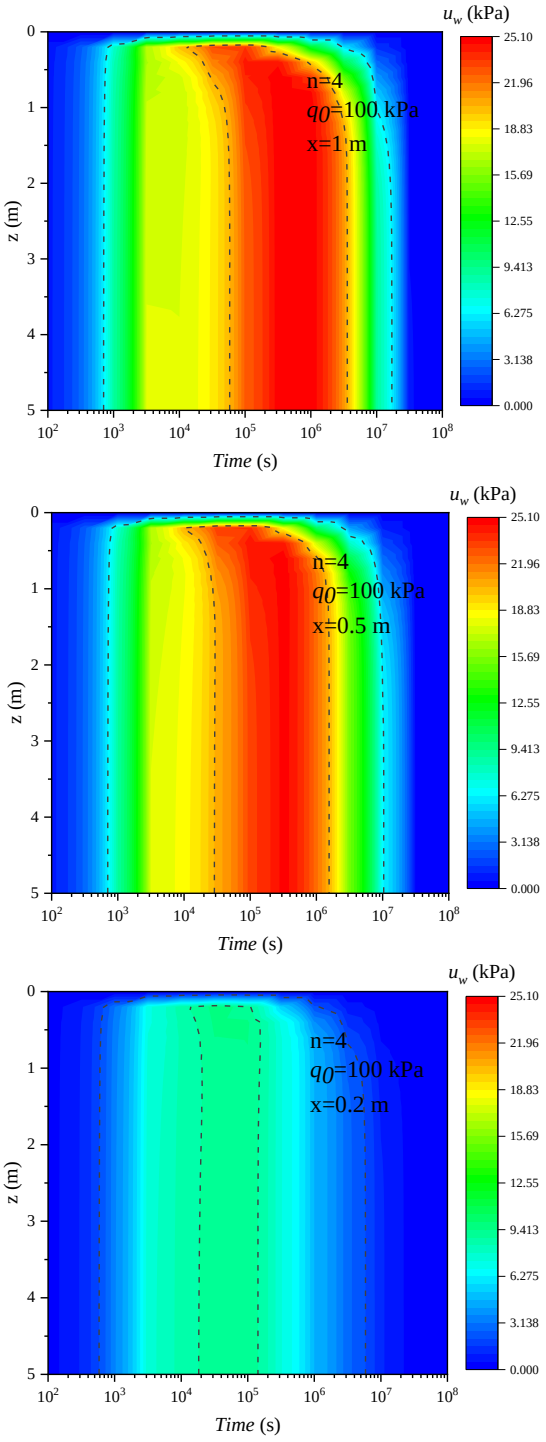

Fig. S6 2D plots of excess pore water pressure varying along the depth of unsaturated soil stratum

Fig. S7 presents non-uniform loads with different values of n and the same value of q_0, which is the reference model of Section 5. 2.

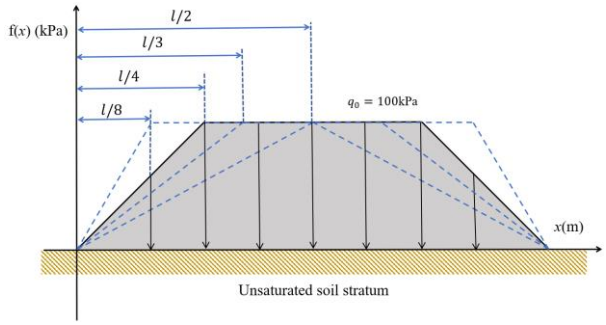

Fig. S7 A mathematical model of non-uniform loads at different values of n

Fig. S8 shows 2D plots of settlement considering the stresses that vary with width x and loading parameters n. Fig. 11 shows the image drawn using Origin drawing software with time as the y-axis of the image and the width of the 2D plane as the x-axis. Using time as the axis can better demonstrate the overall settlement with time under trapezoidal loading.

From Fig. 3 and Fig. 4, it can be seen that the unsaturated soils under the pavement not only have higher excess pore pressure, but also dissipates late. Settlement is caused by pore pressure dissipation, so the final settlement of the pavement is greater than the final settlement of the shoulder, and the settlement of the pavement starts later. During the settlement process, the settlement at the center of the pavement from $t = 10^4 s$ is significantly slower than that under both sides of the pavement. This is because the excess pore pressure reaches its peak successively from $t = 10^4 s$ onwards. Since the values of q_0 are the same, the final settlement under the pavement is the same. The smaller the width of the shoulder, the larger the settlement difference between the shoulder and the pavement.

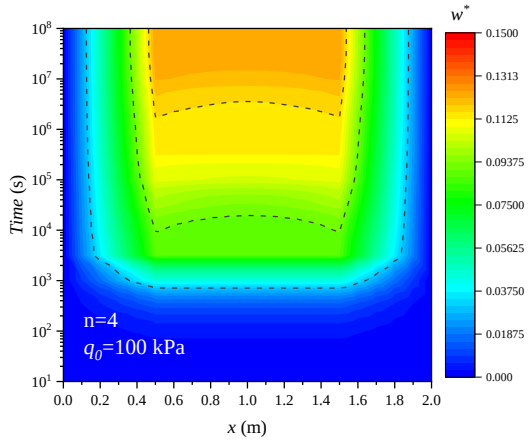

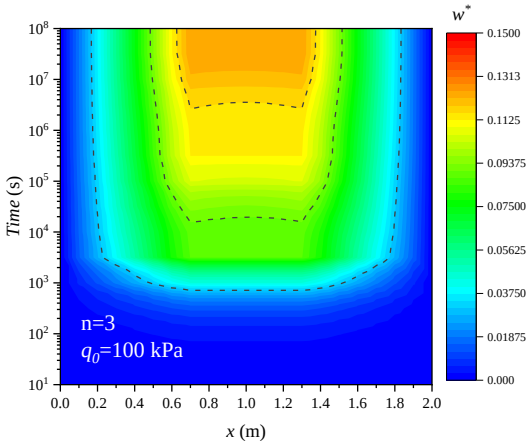

Fig. S8 2D plots of settlement considering the stresses that vary with width and loading parameters n

Fig. S9 shows non-uniform loads at different values of q_0, which is the reference model of Section 5.3.

Although the pore pressure under the shoulder increases proportionally with the increase in roadbed height, the pore pressure under the shoulder is originally much smaller than that under the road surface. Therefore, the increase in the height of the roadbed will lead to an increase in the difference between the pore pressure under the shoulder and that under the road surface. As shown in Fig. S10. Starting from $t = 10^3 s$, the larger the value of q_0, the larger the settling difference. And as time progresses, the settling difference becomes larger and larger. Therefore, when high-fill embankments are used in construction projects, the settlement of the roadbed should be strictly tested. And high fill embankment needs to adopt the construction method of filling in layers and compaction in layers.

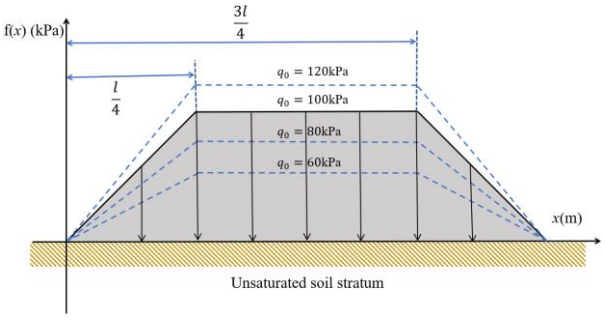

Fig. S9 A mathematical model of non-uniform loads at different values of q_0

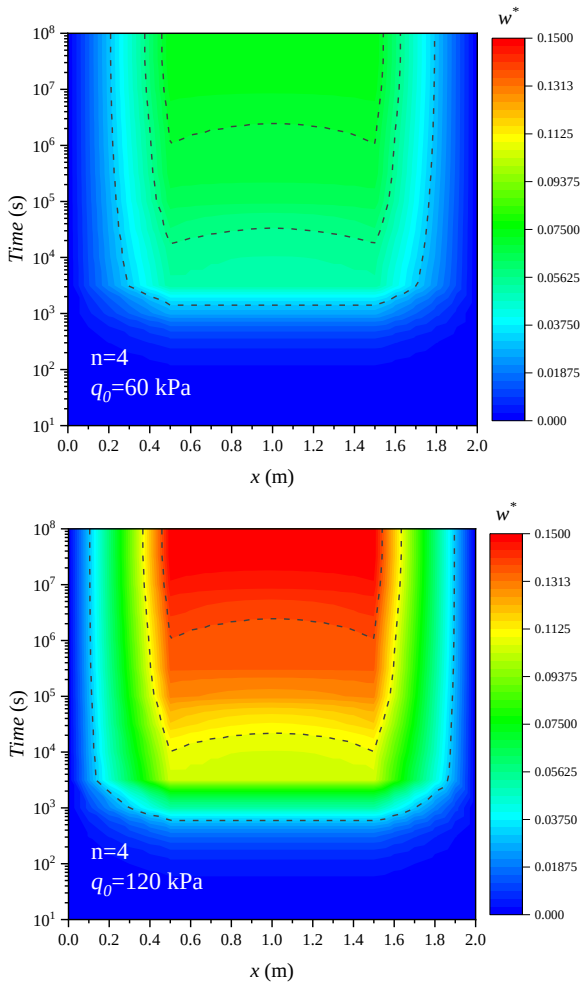

Fig. S10 2D plots of settlement considering the stresses that vary with width and loading parameters q_0

In roadbed construction, the gradient of the side slope will not only affect the stability of the roadbed, but also affect the engineering cost. Therefore, the effect of roadbed slopes is also analyzed in electronic supplementary materials (ESM). Fig. S11 depicts the simplified model of non-uniform loading at different slopes and the same values of load. Fig. S12 presents the influence of different gradients of roadbed slopes on the pore pressure. Actually, the embankment slope is changing when the effect of shoulder width and embankment height are studied in Sections 5.1 and 5.2. In order to separate the effect of roadbed slope, the area of the trapezoidal load maintain the same. This value is $75 \cdot l\ (kPa)$. As shown in Fig. S12, the excess pore pressure under the pavement to increase with the value of q_0. When the slope of the load increases, the excess pore pressure under the shoulder increases together. Since the load under the road shoulder is small, the effect of slope under the road shoulder is not significant.

Fig. S13 shows 2D plots of settlement under loads at the different slopes. The parameters q_0 and n have been marked in Fig. S13. At the same total load value, the larger the slope, the closer the load of the roadbed is to the uniform load. This also makes the difference between the final settlement at the pavement and the road shoulder smaller. During settlement, the pore pressures cause the settlement rate at the pavement to be different. The more uniform the load is, the less significant the difference in settlement rate is. In the actual project, the height and slope of the embankment will be changed for the actual needs. To avoid subgrade defect such as roadbed subsidence and longitudinal cracking of the roadbed, pre-compaction consolidation of the ground surface is required.

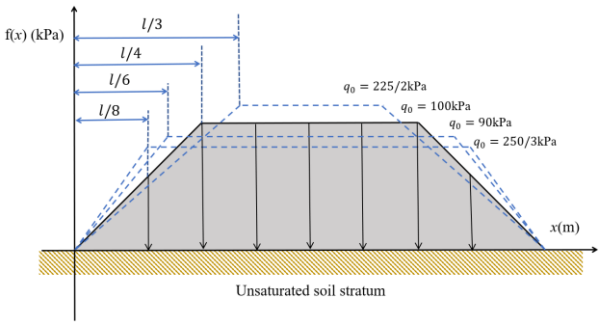

Fig. S11 A mathematical model of non-uniform loading at different shapes and the same value of loads

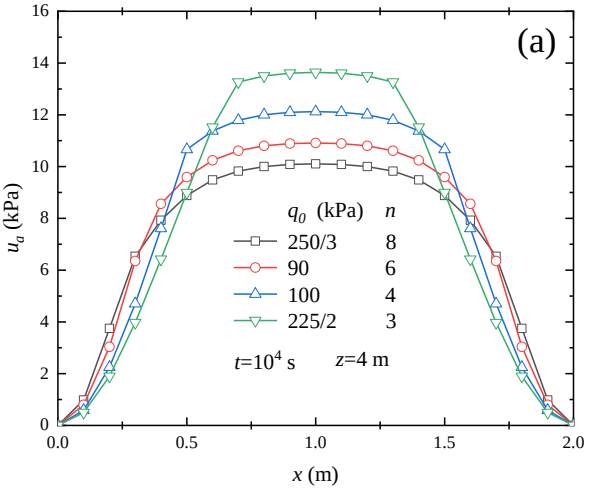

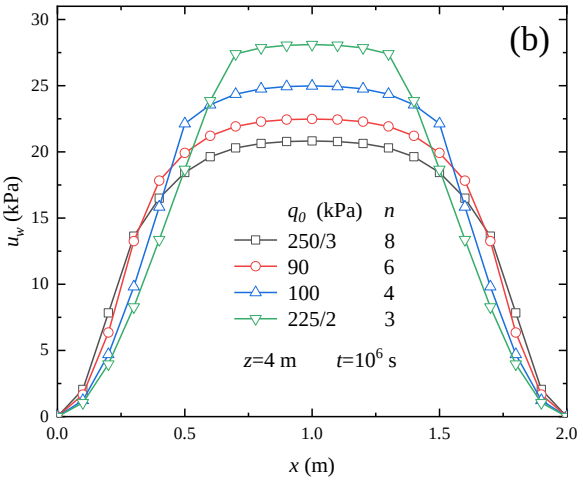

Fig. S12 Effect of different slopes on the (a) excess pore-air pressure; and (b) excess pore-water pressure under non-uniform loads

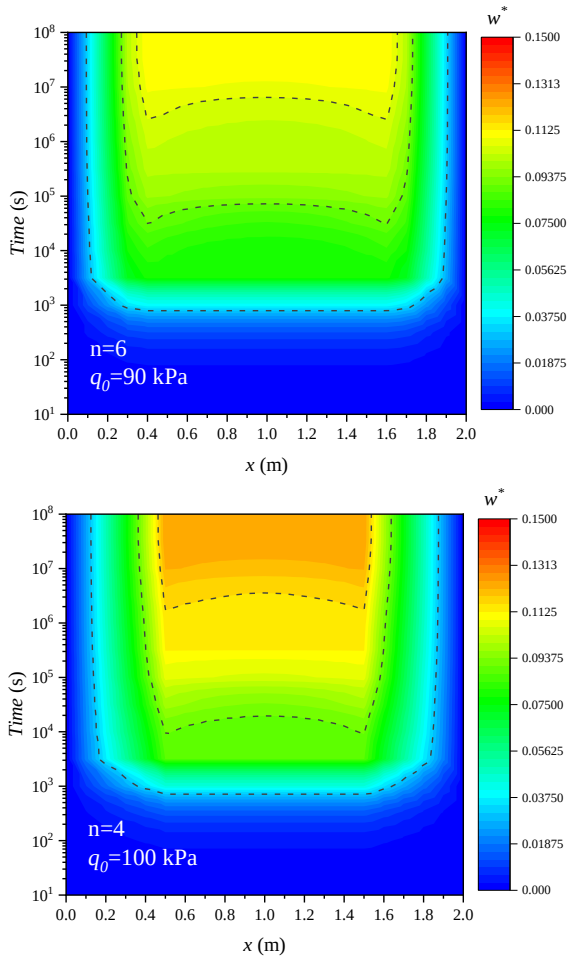

Fig. S13 2D plots of settlement under loads of different shapes for the same area